# Check for updates

#### **OCEANOGRAPHY**

# Declining ocean greenness and phytoplankton blooms in low to mid-latitudes under a warming climate

Zhongkun Hong<sup>1,2</sup>, Di Long<sup>1,2</sup>\*, Kaiyue Shan<sup>1,2</sup>\*, Jian-Min Zhang<sup>1,2</sup>, R. lestyn Woolway<sup>3</sup>, Maofeng Liu<sup>4</sup>, Michael E. Mann<sup>5</sup>, Hongwei Fang<sup>1,6</sup>\*

Marine phytoplankton are crucial to oceanic ecosystems, yet trends in their activity, monitored through chlorophyll a, remain uncertain due to observational limitations. We generated an ocean chlorophyll a dataset (2001 to 2023) across low to mid-latitudes (45°N to 45°S) using multisource data and a deep learning approach. Our analysis suggests widespread decline in ocean greenness, with chlorophyll a concentrations decreasing at a rate of  $(-0.35 \pm 0.10) \times 10^{-3}$  milligrams per cubic meter per year (mg m<sup>-3</sup> year<sup>-1</sup>). The decline is steeper in coastal regions [ $(-0.73 \pm 0.22) \times 10^{-3}$  mg m<sup>-3</sup> year<sup>-1</sup>]. The frequency of high chlorophyll a concentration events in coastal waters has decreased at a relative rate of -1.78% per year. These trends are predominantly driven by rising sea surface temperatures, which enhance ocean stratification, suppress nutrient upwelling, and limit phytoplankton growth. These findings suggest a long-term decline in marine primary production and a reduced occurrence of phytoplankton blooms, potentially disrupting trophic interactions and oceanic carbon cycling.

Copyright © 2025 The Authors, some rights reserved; exclusive licensee American Association for the Advancement of Science. No claim to original U.S.
Government Works.
Distributed under a Creative Commons Attribution
NonCommercial
License 4.0 (CC BY-NC).

#### INTRODUCTION

Marine phytoplankton, responsible for nearly half of the biosphere's net primary productivity (1), play a crucial role in the marine carbon cycle and Earth's climate system (2, 3). Regions with high phytoplankton activity are hotspots for primary production (PP), supporting marine fisheries and broader ecosystems (4–6). However, excessive proliferation of harmful algae can cause severe environmental issues (7). These dynamics underscore the need for long-term, consistent, and global-scale monitoring of marine phytoplankton biomass.

Chlorophyll a (Chl-a), the primary pigment involved in phytoplankton photosynthesis (8-10), is widely used as a proxy for phytoplankton biomass (2, 11–13). However, the magnitude and direction of global phytoplankton biomass trends remain contentious due to inconsistencies in observational data and methods (7, 12, 14-20). Ship-based measurements suggest a century-long decline in phytoplankton biomass, corroborated by early satellite observations (2, 14). Studies indicate that an intensification of ocean stratification, driven by rising sea surface temperature (SST) due to anthropogenic global warming, can lead to depleted nutrient stores in the near-surface layer (Fig. 1A), leading to reduced phytoplankton biomass, particularly in mid- and low-latitude regions (19, 21-23). In contrast, some research links rising SST to enhanced algal blooms in coastal areas (7, 24, 25), suggesting a greening of the oceans at low latitudes (12, 18). While progress has been made in understanding these patterns, the lack of standardized methodologies and inconsistencies in the available data hinder definitive conclusions (15, 26, 27).

While satellite datasets provide long-term, large-scale observations (12), relying on them alone presents notable challenges (28, 29).

For instance, up to 70% of global ocean color data from the Moderate Resolution Imaging Spectroradiometer (MODIS) onboard NASA's Aqua satellite are missing due to, among others, cloud cover, sun glint, or high viewing angles (30–32). In addition, ocean color retrieval algorithms are often inaccurate in turbid coastal regions (28, 29). Data reconstruction methods developed to address these gaps (33–37) are typically constrained by the spatiotemporal resolution of the original datasets and may overlook environmental drivers of Chl-a dynamics. In situ measurements, while oftentimes extensive, suffer from inconsistent sampling standards and uneven spatiotemporal distributions (15, 26, 27). These limitations hinder accurate assessment of spatiotemporal patterns in ocean Chl-a concentrations, particularly in coastal regions where ecosystems are highly sensitive to shifts under oceanographic conditions (38).

To address these challenges, we present the first consistent spatial and temporal estimates of daily Chl-a concentrations across low- to mid-latitude oceans (45°N to 45°S) from 2001 to 2023 using deep learning algorithms (Fig. 1B). We developed the Ocean Chl-a reconstruction Neural Ensemble Network (OCNET) model (Materials and Methods), which integrates key environmental factors influencing phytoplankton growth (fig. S1), satellite observations, and BGC-Argo data (table S1). The OCNET model produces a daily Chl-a dataset with a 0.25° by 0.25° spatial resolution across low- to mid-latitude oceans and demonstrates strong agreement [coefficient of determination ( $R^2$ ) = 0.93, relative bias (RB) = 4.09%] with satellite-based data (Fig. 1C).

#### **RESULTS**

## Chl-a trends for low- to mid-latitude oceans from 2001 to 2023

The low- to mid-latitude oceans are becoming progressively less green, with Chl-a concentrations exhibiting a significant decline from 2001 to 2023 at a mean annual rate of decrease of  $(0.35\pm0.10)\times10^{-3}$  mg m $^{-3}$  year $^{-1}$  (Fig. 2). Coastal regions have experienced an even more pronounced decline, at an average rate of  $(-0.73\pm0.22)\times10^{-3}$  mg m $^{-3}$  year $^{-1}$ , about double the global average (45°N to 45°S), with the most significant reductions observed near river estuaries. In the

<sup>&</sup>lt;sup>1</sup>State Key Laboratory of Hydroscience and Engineering, Department of Hydraulic Engineering, Tsinghua University, Beijing 100084, China. <sup>2</sup>Institute of Ocean Engineering, Tsinghua University, Beijing 100084, China. <sup>3</sup>School of Ocean Sciences, Bangor University, Menai Bridge, Anglesey, UK. <sup>4</sup>Department of Atmospheric and Oceanic Sciences, School of Physics, Peking University, Beijing 100871, China. <sup>5</sup>Department of Earth and Environmental Science, University of Pennsylvania, Philadelphia, PA, USA. <sup>6</sup>Department of Ocean Science and Engineering, Southern University of Science and Technology, Shenzhen 518055, China.

<sup>\*</sup>Corresponding author. Email: dlong@tsinghua.edu.cn (D.L.); sky\_typhoon@mail. tsinghua.edu.cn (K.S.); fanghw@tsinghua.edu.cn (H.F.)

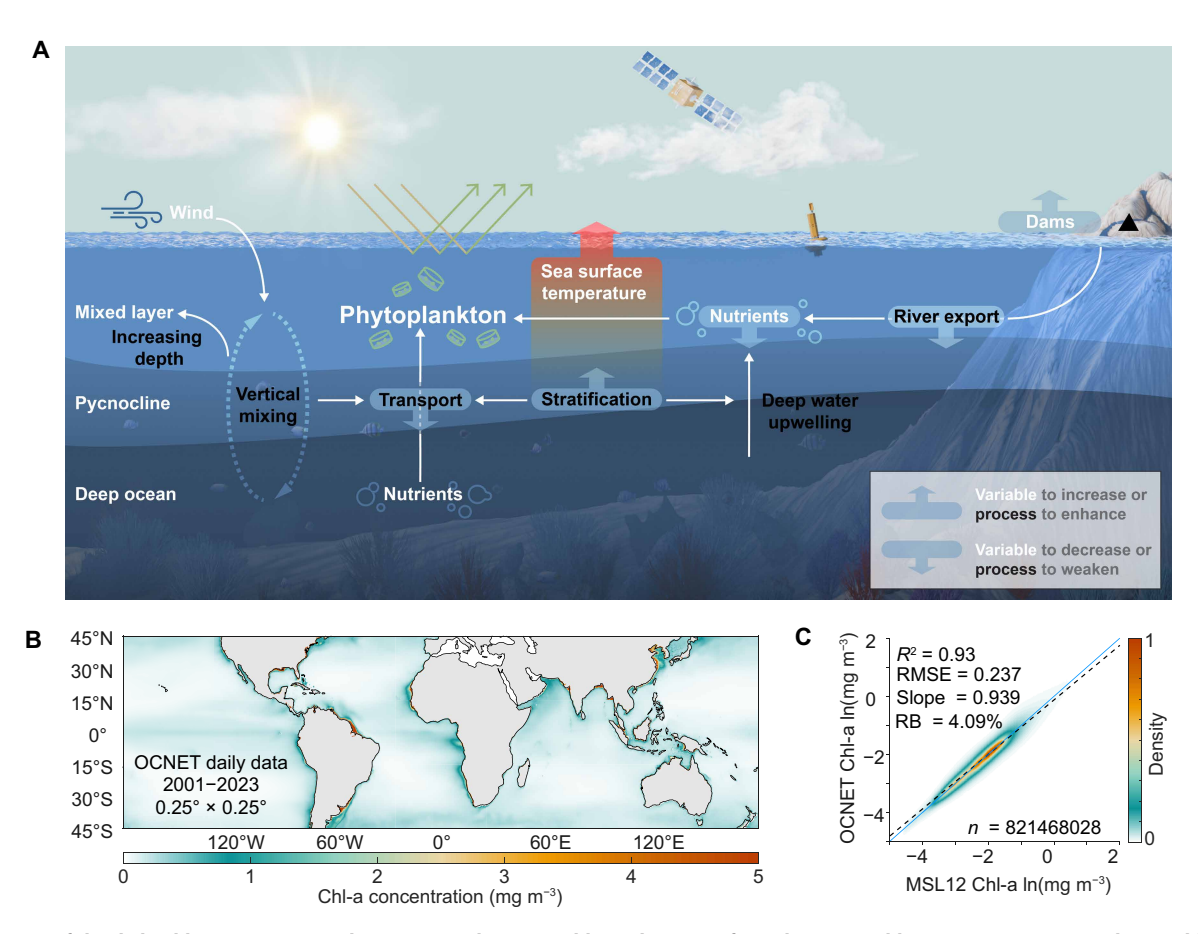


**Fig. 1. Overview of the daily Chl-a concentration dataset across low- to mid-latitude oceans from the Ocean Chl-a reconstruction Neural Ensemble Network model.** (A) Schematic of monitoring techniques and processes regulating marine phytoplankton biomass. Under optimal environmental conditions, phytoplankton growth depends primarily on light and nutrients, influenced by natural and anthropogenic factors, including ocean circulation, mixed-layer dynamics, upwelling, river export, and solar cycles. (B) Spatial distribution of mean Chl-a concentrations spanning 45°N to 45°S from 2001 to 2023, based on the Ocean Chl-a reconstruction Neural Ensemble Network (OCNET) model. This model integrates satellite observations, Biogeochemical Argo (BGC-Argo) data, and key environmental factors using a deep learning approach, producing a global daily Chl-a concentration dataset at a resolution of 0.25° by 0.25°. (C) Log-log scatterplot of space- and time-matched Chl-a concentrations estimated by OCNET and corresponding National Oceanic and Atmospheric Administration (NOAA) Multi-Sensor Level-1 to Level-2 (MSL12) satellite data (Materials and Methods). Pixel color represents data density. The black dashed line indicates the linear regression fit [coefficient of determination (R<sup>2</sup>) = 0.93; P < 0.0001], and the blue solid line represents the idealized 1:1 relationship.

Northern Hemisphere, areas with significant declines are 4.4 times larger than those with significant increases, whereas in the Southern Hemisphere, these areas are approximately equal in extent. Under the influence of upwelling and currents, a westward-expanding Chl-a-enriched region has been observed in the equatorial Pacific Ocean (Fig. 2A) (39). We further analyzed 40 coastal regions based on large marine ecosystem (LME) regions (Materials and Methods). Among these, 40% show a statistically significant declining trend in Chl-a concentration, while only 12.5% exhibit significant increases (figs. S2 and S3).

We define marine high Chl-a (MHC) events as periods of extreme Chl-a concentrations exceeding specific thresholds (90th percentile and 0.2 mg/m³) within a limited time frame (Materials and Methods). Between 2001 and 2023, we observed a substantial reduction in the frequency of MHC events across most coastal regions, with an overall decline of 1.78% per year (Fig. 2E). Regions with significant decreases in MHC events outnumber those with increases by a factor of 4.5. The spatial pattern reveals more pronounced declines near the equator and midlatitudes, with relatively lower

rates between 15° and 30° latitude in both hemispheres. The declining trends in coastal MHC events align closely with changes in Chla concentrations in key regions such as the eastern United States, West Africa, and East Asia (Fig. 2). Areas with higher Chl-a concentrations generally exhibit more pronounced reductions in MHC event frequency (fig. S2). Despite the overarching low- to mid-latitude decline, certain regions, such as the North Brazil Shelf, Canary Current, and Northeast Australian Shelf, show increases in MHC events. These localized trends are likely due to intensified human activities, including increased nutrient exports that elevate Chl-a concentrations (40, 41).

### Climate effects on Chl-a concentrations

Phytoplankton growth in low- to mid-latitude oceans is primarily constrained by nutrient availability (42, 43). Nutrients are typically transported from deeper ocean layers to the upper ocean via vertical mixing and upwelling; however, the pycnocline at the base of the mixed layer acts as a barrier, limiting these nutrient supply processes (2, 44). Recent decades have seen intensified ocean stratification,

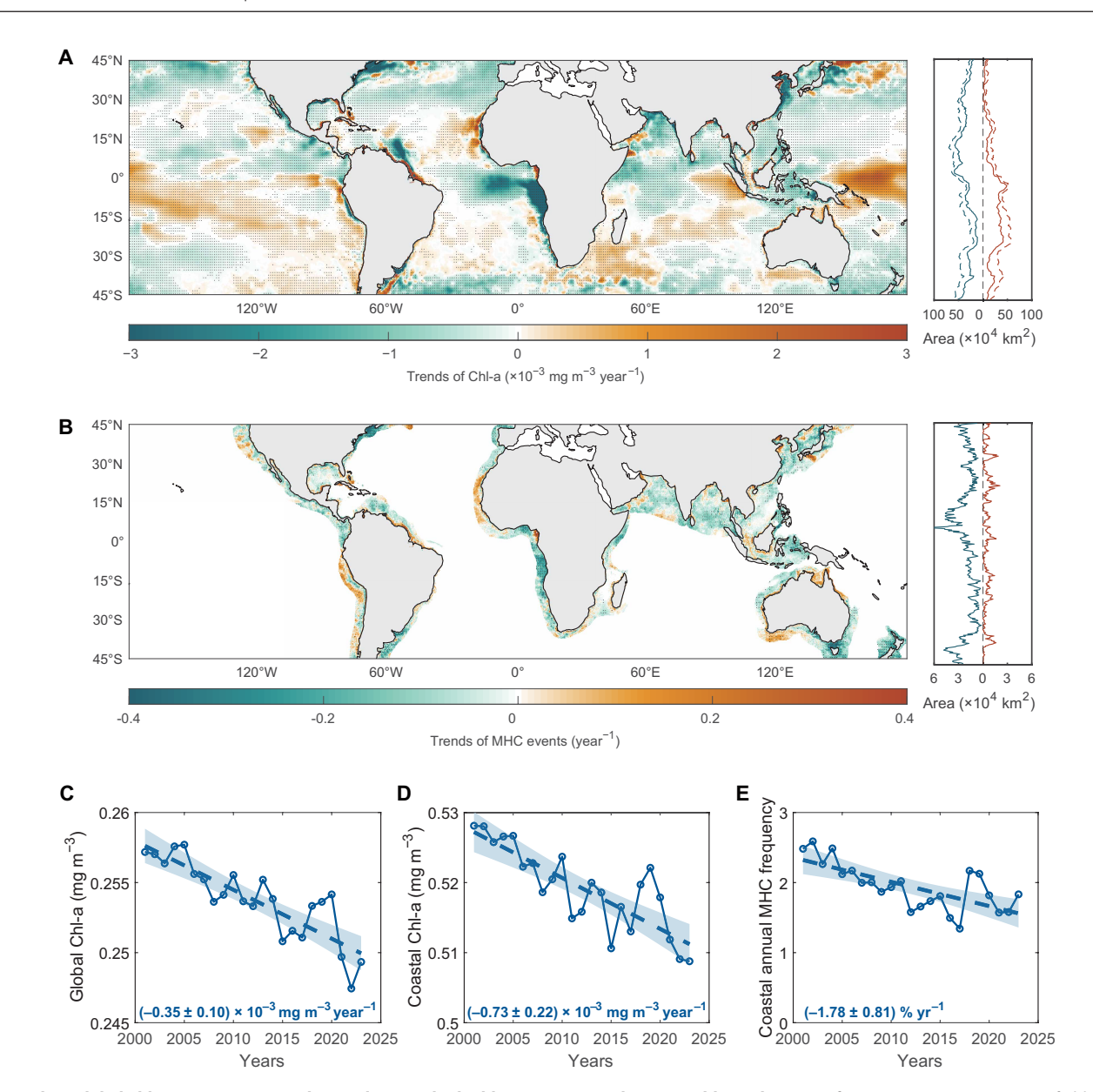


Fig. 2. Trends in global Chl-a concentration and coastal marine high Chl-a events across low- to mid-latitude oceans from 2001 to 2023. (A) Map of Chl-a concentration trends between 45°N and 45°S, with 32.4% of the ocean area showing a significant decrease and 17.6% showing a significant increase (95% confidence level). Black dots indicate areas where trends are statistically significant. Latitudinal profiles depict the total area with significant trends (solid lines) and all trends (dashed lines) along the east-to-west direction, with red and blue representing positive and negative trends, respectively. (B) Trends in coastal marine high Chl-a (MHC) events, with 21.6% of coastal regions exhibiting a significant decrease and 5.0% showing a significant increase (95% confidence level). Coastal boundaries are defined on the basis of LME regions (Materials and Methods). (C and D) Time series of mean Chl-a concentration for low to mid-latitudes (45°N to 45°S) (C) and coastal regions (D). Solid lines represent annual averages, and dashed lines represent linear trends. Shaded areas denote the 95% confidence intervals of the regression analysis. (E) Time series of the annual frequency of coastal MHC events (solid lines) and their linear trend (dashed lines).

driven by a more rapid warming of the upper ocean compared to deeper layers due to global climate change (45, 46). This increased stratification is likely weakening vertical nutrient transport and thus limiting nutrient availability for phytoplankton growth in the upper ocean. The sharp decline in Chl-a concentration in the equatorial Atlantic Ocean is closely related to the limitations in nutrient acquisition (Fig. 2A) (44). To evaluate the role of upper-ocean warming in these dynamics, we examine the relationship between changes in SST and Chl-a concentrations. Globally, the Pearson correlation coefficient

between SST and Chl-a time series is -0.81 (P < 0.01), underscoring the notable role of rising SST in influencing Chl-a dynamics (fig. S4) (2, 3, 16).

The frequency of MHC events appears to be more sensitive to global warming than mean Chl-a concentrations (fig. S5). To explore the relationship between SST and the frequency of MHC events, we removed the annual trend, seasonal cycles, and autocorrelation from the data (Materials and Methods and fig. S6). Across the globe, 75% of LME regions show significant negative correlations

between SST and MHC event frequency (Fig. 3). This suggests that as SST anomalies rise, intensified ocean stratification suppresses vertical nutrient transport (42, 45), thereby reducing the occurrence of MHC events in coastal waters. Vertical mixing may also play a supplementary role in regulating MHC events (24, 46). Approximately 42% of coastal regions exhibit significant positive correlations between MHC event frequency and changes in mixed-layer depth (MLD) (figs. S7 and S8). This indicates that deeper mixing

can occasionally mitigate the impacts of stratification by bringing nutrients to the upper ocean, sustaining phytoplankton growth. However, these effects are region specific and context dependent. Human activities further complicate nutrient dynamics in coastal regions. Some regions with significant positive correlations between MHC event frequency and SST anomalies are heavily influenced by human activities (40, 41), such as nutrient inputs from river discharge (5, 22). For instance, the North Brazil Shelf is notably affected

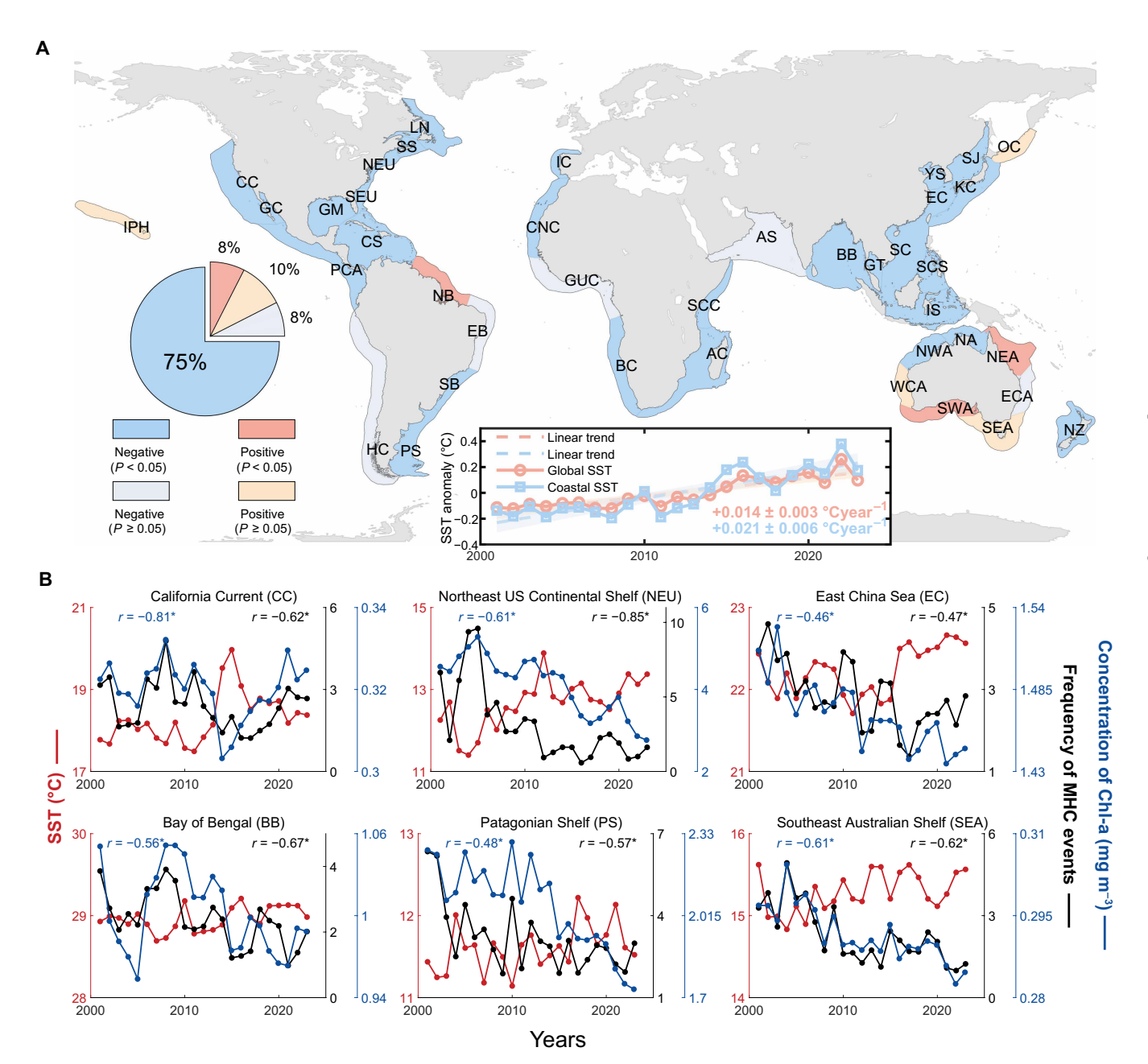


Fig. 3. The role of global warming on MHC events. (A) Correlation between SST and MHC event frequency after removing annual trends, seasonal cycles, and autocorrelation (Materials and Methods). The pie chart indicates the proportions of regions with significant or insignificant positive and negative correlations. Below, time series of SST anomalies are shown for the global oceans (45°N to 45°S) and coastal regions. The expanded forms of LME regions are listed in table S2. (B) Time series of SST, MHC event frequency, and Chl-a concentrations in six coastal regions: the California Current, Northeast US Continental Shelf, East China Sea, Bay of Bengal, Patagonian Shelf, and Southeast Australian Shelf. Pearson correlation coefficients (r) between MHC event frequency and Chl-a concentration with SST are indicated. Asterisks denote statistically significant correlations at the 95% confidence level.

by deforestation and wildfires in the adjacent Amazon basin (47), which alter nutrient fluxes through runoff and atmospheric deposition. Similarly, the Northeast Australian Shelf faces nutrient enrichment challenges linked to poor water quality management in the Great Barrier Reef catchment (41). These anthropogenic contributions underscore the dual role of natural and human-driven processes in shaping Chl-a dynamics in coastal ecosystems.

#### **Implications for PP**

Chl-a serves as a reliable indicator of marine PP (3, 11) and plays a critical role in regulating oceanic biological processes and global carbon dynamics. In this study, we used the well-established vertically generalized production model (VGPM) (3, 11, 48) to estimate PP using Chl-a data derived from the OCNET model, along with SST and photosynthetically active radiation (Materials and Methods). Our analysis suggests a significant decline in marine PP across low- to mid-latitude (45°N to 45°S) regions at a rate of -0.088% per year  $[-0.032 \pm 0.025 \text{ billion tonnes (Gt) C year}^{-1}$ ; Fig. 4A] consistent with the observed downward trend in Chl-a concentrations (Fig. 2). Notably, coastal regions exhibit an accelerated decline in PP at a rate of -0.145% per year  $(-0.015 \pm 0.008 \text{ Gt C year}^{-1}; \text{ Fig. 4B})$ , with a relative rate approximately 60% higher than the global average. These findings align with previous studies on global PP (3, 38, 44) but show variability in magnitude due to differences in spatial and temporal coverage. The more pronounced decline in coastal PP

emphasizes the vulnerability of these regions to recent climatic and anthropogenic changes. Our results differ from earlier studies based on ship measurements and earlier satellite datasets, which suggested a slower decline or even increasing rates of Chl-a in coastal regions compared to offshore areas (14). This discrepancy may stem from differences in data sources, temporal coverage, and the intensifying impacts of climate change on coastal ecosystems (23, 49, 50). In recent years, coastal regions have experienced nutrient transport restrictions due to dam construction and less river export (Fig. 1A) (5, 51, 52), which are likely exacerbating declines in Chl-a and PP. The globally consistent spatiotemporal coverage of our Chl-a dataset enables more comprehensive insights into these dynamics, offering valuable information for understanding climate change impacts on marine ecosystems and informing ocean management strategies.

#### DISCUSSION

Globally, definitions and evaluation metrics for algal blooms remain inconsistent (7), with various approaches relying on Chl-a anomalies (11) or various spectral indices (7, 53, 54) for bloom detection. The proliferation of algae, which leads to algal blooms, is typically associated with a marked increase in Chl-a concentration. However, this relationship can vary depending on algal species composition and dynamic environmental conditions. In this study, we assessed the effectiveness of MHC events as indicators of algal blooms by

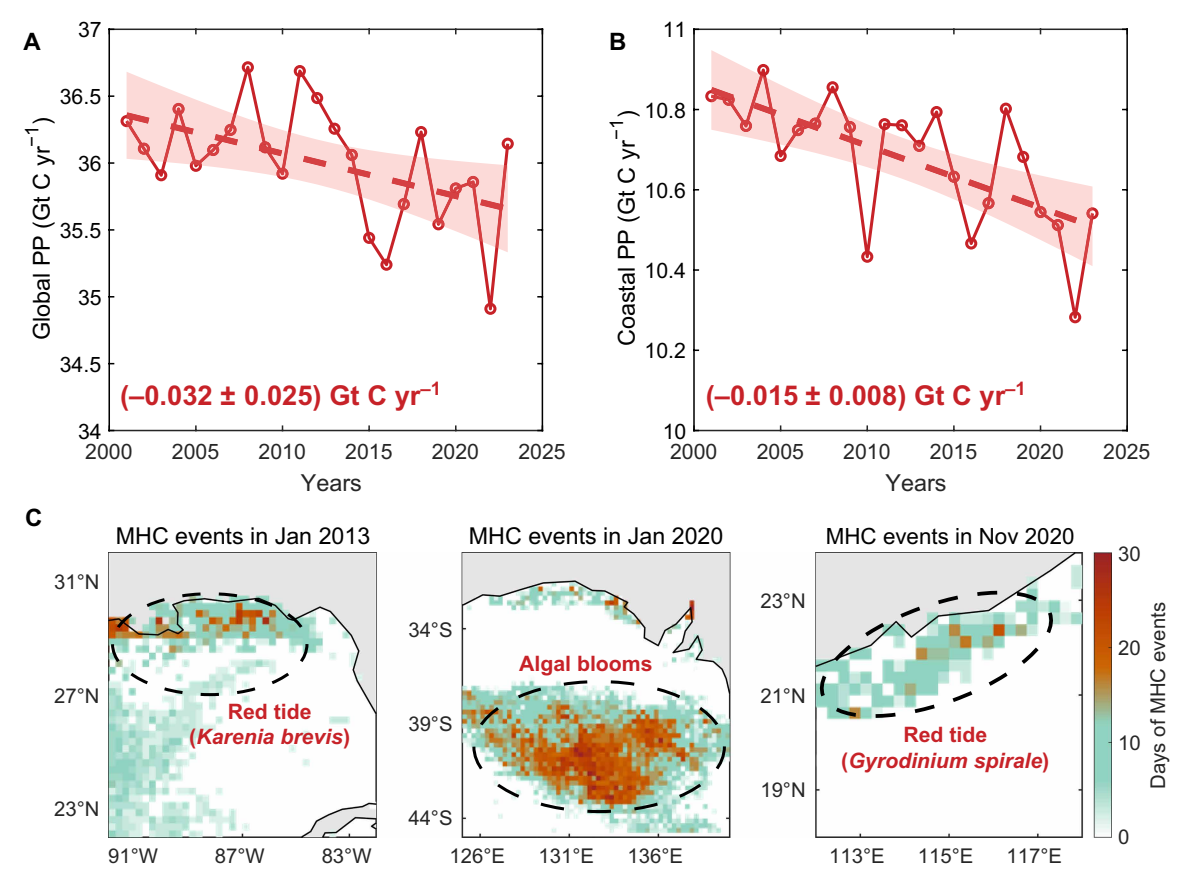


**Fig. 4. Marine PP and algal bloom events.** (**A** and **B**) Time series of mean marine PP (solid lines) and its trends (dashed lines) for the global oceans (45°N to 45°S) (A) and coastal regions (B), calculated using the VGPM based on Chl-a concentrations, SST, and photosynthetically active radiation (PAR). (**C**) Examples of coastal MHC events, with circles indicating the range associated with historical algal bloom events as reported in previous studies (11, 78, 79).

comparing three events from different marine regions. Our results demonstrate that MHC events are effective proxies for identifying algal blooms (Fig. 4C and fig. S9). Leveraging the Chl-a data derived from the OCNET model, we were able to monitor the bloom formation process on a daily timescale, providing unprecedented temporal resolution. Moreover, our application of a "relative high-value" filtering approach minimized interference from suspended sediments and colored dissolved organic matter (28, 29), enabling more accurate detection of Chl-a anomalies. Variations in the definition of algal blooms based on Chl-a concentrations do not influence the observed trends or conclusions of this study, as our evaluation metrics were consistently applied across spatial and temporal scales. Our findings reveal a negative correlation between the frequency of algal bloom events, as indicated by MHC events, and SST (Fig. 3), suggesting that climate change-induced, intensified ocean stratification continues to impede nutrient transport in coastal regions (25, 45, 46, 55).

While three recent studies have reported increases in both the total number of algal bloom events and the peak Chl-a concentrations globally, our findings differ considerably (7, 26, 56). This discrepancy is largely attributable to differences in datasets; the aforementioned studies relied on datasets with incomplete spatial and temporal coverage, such as the MODIS-Aqua satellite dataset, which has more than 70% data gaps (30, 32). Consequently, many algal bloom events would inevitably be missed in those analyses. Furthermore, the reported increases are predominantly driven by contributions from mid- and high-latitude oceans (56), whereas most low-latitude regions, particularly in the Northern Hemisphere, exhibit a declining trend (7, 57), consistent with our results. While we acknowledge that algal blooms in certain regions have intensified, causing severe environmental impacts, and that enhanced monitoring has increased bloom detection (26), our results suggest that the overall global occurrence of algal blooms is declining.

A key contribution of our study is the development of a globally consistent, daily Chl-a concentration dataset generated using deep learning algorithms. This dataset exhibits spatiotemporal continuity and satellite-like quality, enabling robust trend analysis. Our findings show a significant decline in Chl-a concentrations  $[(-0.35 \pm 0.10) \times$ 10<sup>-3</sup> mg m<sup>-3</sup> year<sup>-1</sup>] across low to mid-latitudes, with a more pronounced decrease in coastal regions  $[(-0.73 \pm 0.22) \times 10^{-3} \text{ mg m}^{-3}]$ year<sup>-1</sup>]. In addition, the annual frequency of MHC events exhibits a notable downward trend  $(-1.78\% \text{ year}^{-1})$  under the influence of climate change. These results establish a clear link between declining global ocean Chl-a concentrations, coastal MHC events, and increasing SST, suggesting that a warmer upper ocean (and likewise a strengthening of stratification) is likely to result in reduced global marine PP (38, 44) and fewer phytoplankton blooms. These changes will profoundly affect the magnitude and distribution of marine ecosystem functioning (12, 58).

## **MATERIALS AND METHODS**

#### Target data preparation and calibration

In this study, satellite-derived data corrected with in situ measurements served as the target dataset for the OCNET model, ensuring high-quality simulations. Specifically, the National Oceanic and Atmospheric Administration (NOAA) Multi-Sensor Level-1 to Level-2 (MSL12) dataset was used as the primary training data source for the OCNET model (59) (https://coastwatch.noaa.gov/cwn/product/

noaa-msl12-multi-sensor-dineof-global-9km-gap-filled-products-chlorophyll-diffuse.html). This dataset provides near real-time, gap-free global Chl-a concentration maps by merging data from Visible and Infrared Imaging Radiometer Suite (VIIRS) and OLCI-Sentinel-3A satellites, with gaps filled using the Data Interpolating Empirical Orthogonal Function method. The MSL12 dataset offers broad spatial coverage, revealing intricate marine features in coastal and inland waters. However, its temporal coverage is limited to post–9 February 2018 (table S1). To correct biases in the MSL12 dataset, Chl-a measurements from the BGC-Argo program were used. BGC-Argo extends the Argo program by collecting ocean biogeochemical parameters, including Chl-a, alongside physical variables such as temperature, salinity (SAL), and pressure (https://biogeochemical-argo.org/data-access.php). Only "good data" profiles with delayed-time calibrated values were included in this study.

The calibration process comprised two steps: (i) determining the optimal depth for matching BGC-Argo and satellite data and (ii) correcting the MSL12 data using artificial neural networks (ANN; fig. S1). Chl-a concentrations from BGC-Argo are measured at various depths during the float's descent and ascent, while satellite data represent surface ocean conditions, typically within the upper mixed layer. As Chl-a distribution varies with depth and location, optimal depth matching is critical for accurate calibration. The optical depth was identified by minimizing the absolute deviation between MSL12 data and the average BGC-Argo Chl-a concentration at specific depths. To enhance reliability and mitigate outlier influence, we used an ANN trained on geographic coordinates (longitude and latitude) and MLD variables (MLD001 and MLD003; table S1) from the Ocean Reanalysis System 5 (ORAS5) reanalysis dataset (https:// cds.climate.copernicus.eu/datasets/reanalysis-oras5?tab=overview). The best-performing ANN architecture, based on validation accuracy, consisted of three hidden layers with 5, 10, and 5 neurons, respectively. This approach ensured consistent optimal matching depths within the same grid cell, yielding a unified spatial map of

Using the optimal depth map, we recalculated surface Chl-a concentrations from BGC-Argo data, referred to as BGC-Argo (corrected). These values served as the benchmark for calibrating the MSL12 dataset. Given that satellite-derived Chl-a estimates often exhibit biases, especially in turbid coastal areas (29, 32, 60), ANN-based correction was applied. Input variables included latitude, longitude, MLD variables, and the original MSL12 Chl-a values. Data were split into training (70%), validating (15%), and testing (15%) sets. The optimal ANN architecture for this step had three hidden layers with 20, 20, and 13 neurons, respectively. Following the correction, the  $R^2$  value between MSL12 and BGC-Argo data improved from 0.41 to 0.78, while the root mean square error (*RMSE*) decreased from 0.75 to 0.55.

To ensure spatial continuity of the corrected MSL12 data, we used an inverse distance weighting (IDW) fusion algorithm. BGC-Argo correction influence was limited to a 500-km radius, with weights decreasing exponentially with distance (Eq. 1). The corrected Chl-a concentration for each grid cell (Eq. 2) incorporated data from all BGC-Argo sites within this radius. The final corrected dataset spans 9 February 2018 to 31 December 2023, offering high spatiotemporal continuity and improved accuracy for global Chl-a monitoring

Weight<sub>D</sub> = 
$$e^{-D/(R/5)} - e^{-5}$$
 (1)

$$C_{\rm cor} = \sum C_{\rm argo\_cor} \times Weight_D + C_{\rm msl} \times \left(1 - \sum Weight_D\right) \ (2)$$

where  $Weight_D$  is the weight of a grid cell at distance D (in kilometers) from a BGC-Argo site. R is the maximum distance range (500 km;  $D \le R$ ).  $C_{\rm cor}$  is the corrected Chl-a concentration for the grid cell.  $C_{\rm argo\_cor}$  is the Chl-a concentration from BGC-Argo sites within the influence range.  $C_{\rm msl}$  is the original MSL12 Chl-a concentration for the grid cell.

#### **OCNET** model architecture

This study uses Chl-a data derived from the updated OCNET model (fig. S1), an ensemble convolutional neural network architecture designed for reconstructing global sea surface Chl-a concentration. The OCNET model integrates environmental variables related to phytoplankton growth, enabling the generation of spatially and temporally complete Chl-a concentration datasets (61). The model primarily incorporates SAL, SST, sea surface pressure (SSP), and MLD from reanalysis datasets, as well as photosynthetically active radiation (PAR) and Chl-a concentration data from satellite datasets (fig. S1 and table S1). While these variables capture the key drivers of phytoplankton dynamics, certain anomalous events (11, 41, 62) such as wildfires, land-use changes, and wastewater discharges remain challenging to incorporate directly as inputs. Notably, human-induced impacts vary regionally and are difficult to quantify, potentially leading to localized underestimations of Chl-a (fig. S10). However, these limitations do not compromise the global-scale reliability of OCNET-derived Chl-a estimates, which remain consistent with satellite observations (Fig. 1C and fig. S10). The comprehensive evaluation results reveal that the OCNET model achieves excellent and comparable performance across the training set (RMSE = 0.225), validation set (RMSE = 0.248), and testing set (RMSE = 0.301), ensuring the model's robustness and precluding potential overfitting.

In its initial implementation (61), the OCNET model was designed primarily for open-ocean Chl-a simulations, given the limited availability and lower reliability of satellite-based observations in coastal regions (29, 63). Coastal areas, such as the East China Sea, often suffer from data gaps or high uncertainty in satellite-derived Chl-a estimates (30), rendering their use as training targets unreliable. To enhance the model's performance in these regions, we incorporated BGC-Argo observational datasets to correct the model's target data (Materials and Methods and fig. S1).

Alongside NOAA's MSL12 dataset, the Ocean-Colour Climate Change Initiative (OCCCI) version 6 dataset (https://climate.esa. int/en/) serves as a key satellite-based Chl-a data source for OCNET (64). OCCCI products, derived from multiple sensors, including the European Space Agency's Moderate Spectral Resolution Imaging Spectroradiometer, NASA's Sea-viewing Wide Field-of-view Sensor, MODIS-Aqua, and NOAA's VIIRS, span from 1997 onward (64). However, because OCCCI's daily and monthly data often contain missing values, they cannot be used directly as model inputs. Instead, we used its climatology dataset as a background field to constrain Chl-a concentration estimates within realistic ranges (61). The OCCCI climatology dataset, providing 12 months of valid observational data, is used to generate a continuous baseline for Chl-a from 1 January 2001 to 31 December 2023, through temporal smoothing and interpolation.

The OCNET model relies on five key environmental variables, i.e., SST, SAL, PAR, SSP, and MLD, each of which plays a crucial role

in phytoplankton growth and distribution (2, 3, 7, 65). SST influences algal metabolic rates, enzymatic activity, cell division, and growth cycles, while SAL affects osmoregulation and balance in marine phytoplankton (66), making both variables essential inputs. Hydrodynamic changes in wind patterns and ocean currents can also affect surface algal distribution; to represent this effect, we incorporate SSP as an input variable. The influence of MLD on Chl-a concentrations varies seasonally: In winter, deeper mixing brings nutrient-rich waters to the surface, promoting phytoplankton growth, whereas in summer, a shallower mixed layer restricts nutrient supply, leading to potential declines in Chl-a. The seasonal transition of MLD is thus closely linked to phytoplankton growth cycles. We sourced SSP and SST data from the Fifth Generation of ECMWF Reanalysis (ERA5) (67) (https://cds.climate.copernicus.eu/datasets/ reanalysis-era5-single-levels?tab=overview), while SAL, MLD001, and MLD003 were obtained from the ORAS5 dataset (68) (https:// cds.climate.copernicus.eu/datasets/reanalysis-oras5?tab=overview), to serve as input data for the OCNET model.

PAR, a critical energy source for photosynthesis, influences phytoplankton photosynthetic efficiency, biomass accumulation, and growth dynamics (69). To ensure robust coverage, we selected PAR data from multiple satellite sources, including MODIS-Terra/Aqua and the Visible Infrared Imaging Radiometer Suite (VIIRS) aboard the Suomi National Polar-orbiting Partnership (SNPP) (https:// oceancolor.gsfc.nasa.gov/l3/). Given the inherent spatial gaps and potential biases among different satellite-derived PAR products, we applied preprocessing and fusion techniques to harmonize these datasets (61). We first performed systematic bias calibration for the other two datasets using MODIS-Aqua as the reference. Subsequently, we integrated the three calibrated datasets by calculating their arithmetic mean at grid cells where at least two sources had valid observations, facilitating spatial complementarity. For cells with only one valid dataset, the available value was retained. Last, remaining minor spatial gaps were filled using spline curve interpolation, ensuring consistent data coverage for subsequent analyses (61).

Considering the typical monthly growth cycle of phytoplankton, we calculated the environmental factors influencing marine algal growth by averaging the data from the preceding month. Specifically, SST, SAL, and PAR were averaged over the previous month and used as inputs of the OCNET model. In addition, daily values of SST, SSP, MLD001, and MLD003 were included as separate input variables (fig. S1E).

The study domain spans from 45°N to 45°S, a choice based on data reliability and research logic. High latitudes have notable seasonal satellite data gaps, particularly in sea ice–covered areas where ice severely disrupts data quality. In high-latitude eutrophic regions, phytoplankton growth is limited primarily by light and temperature, with environmental patterns different and more complex than those in low to mid-latitudes. Therefore, we chose low- to mid-latitude oceans (45°N to 45°S) as our study region. To optimize computational efficiency while preserving regional characteristics, we divided the global ocean into 405 regions, each measuring 16° by 16° and containing 64 grid cells per side. These regions were divided into 45 horizontal and 9 vertical bands, each independently trained using a U-Net–based deep convolutional neural network. The upper-left grid cell of each region was determined using Eqs. 3 and 4

$$Top = 44.875 - (zy - 1) \times 9.25 \tag{3}$$

$$Left = -179.875 + (zx - 1) \times 8 \tag{4}$$

where the variables *Top* and *Left* represent the latitude and longitude of the uppermost and leftmost parts of the region, respectively. The row number *zy* (ranging from 1 to 9) and column number *zx* (ranging from 1 to 45) define the region's position within the segmentation grid.

To minimize boundary effects introduced by regional segmentation, adjacent regions overlap by 8° latitudinally and 6.75° longitudinally. For these overlapping areas, we applied an IDW method (Eqs. 5 and 6) to compute a weighted average of the model outputs

$$D = \sqrt{(i-C)^2 + (j-C)^2}$$
 (5)

$$W_{i,j} = 1 - D/D_{\text{max}} \tag{6}$$

where D is the distance between a given grid cell and the center of the region, with i and j representing the grid cell's row and column, respectively. The center point C is set at C=32.5. The weight  $W_{i,j}$  is assigned on the basis of the relative distance D, where  $D_{\max}$  represents the maximum possible distance from the center to the four corner grid cells. This approach ensures smooth transitions across regional boundaries, improving the robustness of the final Chl-a estimates.

#### **Definition of MHC events and coastal regions**

In this study, we define MHC events as occurrences when Chl-a concentrations exceed both a reference percentile threshold and an absolute threshold, calculated over the entire time series. Specifically, we use the 90th percentile of the time series combined with an absolute threshold of 0.2 mg/m³. This definition is inspired by the concept of marine heatwaves, where MHC events represent occurrences with defined start and end times (70, 71). Following a similar approach, we consider consecutive occurrences separated by gaps of 2 days or less, followed by another event lasting at least 3 days, as a continuous MHC event. In summary, MHC events are spatiotemporally coherent extreme events, where occurrences exceeding the thresholds on consecutive days or neighboring grid points are treated as part of the same MHC event.

The Chl-a dataset used in this study is generated by the OCNET model, providing satellite-like observations. However, these data exhibit considerable roughness and complexity due to factors including measurement errors, long-tailed distributions, and abrupt system state transitions, all of which contribute to unstable and fluctuating time series (72-74). This variability complicates threshold-based MHC event detection. Previous studies have noted that Chl-a concentration data in nearshore coastal areas exhibit lower elasticity, meaning that concentration variations are relatively stable compared to offshore regions, where Chl-a values are generally lower but more sensitive to threshold selection (75). Given this distinction, we focus our analysis on coastal regions to mitigate the impact of extreme data fluctuations. To further reduce noise and enhance event detection stability, we apply a Gaussian filter ( $\sigma = 0.5$ ) to preprocess the Chl-a concentration data, which smooths out minor fluctuations while preserving the primary signal.

Despite data preprocessing and the selection of lower-elasticity nearshore data, identifying persistent MHC events remains challenging due to the complexity of satellite-like datasets. To ensure robust detection, we set a minimum event duration of 3 days, which

is shorter than the commonly used 5-day threshold for marine heatwaves (71). This adjustment yields a global average of two to five MHC events per year, a range that we consider reasonable based on previous analyses.

The selection of threshold values is a critical factor in event detection. Given the high elasticity of Chl-a data, we avoid using excessively high thresholds, which could lead to a disproportionate number of false detections caused by random fluctuations. Overly stringent thresholds could also exaggerate the effects of data uncertainty on the estimated MHC event frequency. Therefore, after extensive testing, we adopted a combined threshold of the 90th percentile and 0.2 mg/m³, ensuring a balance between robustness and sensitivity. Sensitivity analyses confirm that the primary temporal trends of MHC events remain consistent across different threshold settings (fig. S11), demonstrating the robustness of our approach.

MHC events are not equivalent to phytoplankton bloom events. While phytoplankton blooms are typically based on absolute biomass or cumulative biomass thresholds (76), MHC events are primarily determined by a relative threshold (90th percentile) with an additional absolute cutoff (0.2 mg/m³). This means that MHC events can occur even during periods of low Chl-a concentration (i.e., outside traditional bloom seasons). Although blooms are more frequent in high Chl-a regions and seasons, extreme Chl-a events in low-concentration areas are also ecologically notable and warrant attention.

For coastal analyses, we use the LME framework (77). Among the 66 LMEs worldwide, we focus on low- to mid-latitude LMEs, excluding the Mediterranean Sea, Red Sea, and Persian Gulf due to their unique oceanographic characteristics. A total of 40 LMEs was selected for this study (table S2). LME boundaries are sourced from www.sciencebase.gov/catalog/item/55c77722e4b08400b1fd8244.

## **Autocorrelation removal**

Autocorrelation denotes the dependence between adjacent observations in a time series. Ignoring this dependency in cross-variable correlation analysis may induce spurious significance (56). The core of autocorrelation removal is to disentangle the intrinsic dynamic structure of individual time series from genuine intervariable relationships, thereby ensuring that correlation results reflect authentic causal or synergistic linkages between variables. Here, we assume that both MHC event frequency and SST follow the first-order autoregressive model (Eq. 7) (56)

$$\varepsilon_t = y_t - \phi y_{t-1}, t = 2, 3, 4, \dots, T$$
 (7)

where  $\varepsilon_t$  denotes white noise at time t (free of autocorrelation). Using Eq. 7, the original series  $y_t$  can be transformed into a residual series  $\varepsilon_t$  without autocorrelation, achieving the purpose of autocorrelation removal. The first-order autocorrelation coefficient  $\varphi$  is derived from Eq. 8 (56)

$$\phi = \frac{\sum_{t=2}^{T} (y_t - \overline{y}) (y_{t-1} - \overline{y})}{\sum_{t=1}^{T} (y_t - \overline{y})^2}$$
(8)

#### Calculation of PP

To estimate phytoplankton carbon fixation capacity, we applied a light-dependent, depth-resolved model known as the VGPM (48).

The VGPM simplifies the computation of phytoplankton PP by focusing on surface-layer variables while incorporating depth-resolved considerations. The model primarily relies on three key inputs: SST, PAR, and Chl-a concentration. Phytoplankton carbon fixation, denoted as  $PP_{\rm eu}$ , represents the integrated PP from the ocean surface to the euphotic depth  $Z_{\rm eu}$  and is expressed in milligrams of C per square meter per day. The computation follows Eq. 9

$$PP_{\text{eu}} = 0.66125 \times P_{\text{opt}}^{B} \times \left[ E_0 \div \left( E_0 + 4.1 \right) \right] \times Z_{\text{eu}} \times C_{\text{sat}} \times D_{\text{irr}} \quad (9)$$

where  $P_{\mathrm{opt}}^B$  is the maximum carbon fixation rate per unit Chl-a within the water column [in milligrams of C per milligram of chlorophyll per hour], which is temperature dependent and given by Eq. 10;  $E_0$  is PAR (einstein per square meter per day);  $C_{\mathrm{sat}}$  represents Chl-a concentration (in milligrams per cubic meter);  $Z_{\mathrm{eu}}$  is the euphotic depth, defined as the depth where 1% of surface PAR remains available, derived from Chl-a using Eqs. 11 and 12 (1); and  $D_{\mathrm{irr}}$  is the photoperiod (in hours), determined by latitude, longitude, and date. The temperature-dependent function for  $P_{\mathrm{opt}}^B$  follows

$$P_{\text{opt}}^{B} = -3.27 \times 10^{-8} T^{7} + 3.4132 \times 10^{-6} T^{6} - 1.348 \times 10^{-4} T^{5} + 2.462 \times 10^{-3} T^{4} - 0.0205 T^{3} + 0.0617 T^{2} + 0.2749 T + 1.2956$$
(10)

where T represents SST (°C).

The euphotic depth ( $Z_{eu}$ ) is calculated as

$$Z_{\text{eu}} = \begin{cases} 200 \times C_{\text{tot}}^{-0.293}, C_{\text{tot}} < 10\\ 568.2 \times C_{\text{tot}}^{-0.746}, C_{\text{tot}} \ge 10 \end{cases}$$
 (11)

where the total pigment content ( $C_{tot}$ ) is defined as

$$C_{\text{tot}} = 37.9 \times C_{\text{sat}}^{0.548} \tag{12}$$

For global  $PP_{\rm eu}$  calculations, we used SST data from ERA5, satellite-derived PAR data, and OCNET Chl-a products (table S1). The final global PP estimates were obtained by integrating  $PP_{\rm eu}$  over spatial grids, weighted by corresponding grid areas.

## **Supplementary Materials**

This PDF file includes:

Figs. S1 to S11 Tables S1 and S2

#### **REFERENCES AND NOTES**

- C. B. Field, M. J. Behrenfeld, J. T. Randerson, P. Falkowski, Primary production of the biosphere: Integrating terrestrial and oceanic components. Science 281, 237–240 (1998).
- D. G. Boyce, M. R. Lewis, B. Worm, Global phytoplankton decline over the past century. Nature 466, 591–596 (2010).
- M. J. Behrenfeld, R. T. O'Malley, D. A. Siegel, C. R. McClain, J. L. Sarmiento, G. C. Feldman, A. J. Milligan, P. G. Falkowski, R. M. Letelier, E. S. Boss, Climate-driven trends in contemporary ocean productivity. *Nature* 444, 752–755 (2006).
- S. R. Brody, M. S. Lozier, J. P. Dunne, A comparison of methods to determine phytoplankton bloom initiation. *J. Geophys. Res. Oceans* 118, 2345–2357 (2013).
- S. P. Seitzinger, E. Mayorga, A. F. Bouwman, C. Kroeze, A. H. W. Beusen, G. Billen, G. Van Drecht, E. Dumont, B. M. Fekete, J. Garnier, J. A. Harrison, Global river nutrient export: A scenario analysis of past and future trends. *Global Biogeochem. Cycles* 24, GB0A08 (2010).
- K. Filbee-Dexter, A. Pessarrodona, M. F. Pedersen, T. Wernberg, C. M. Duarte, J. Assis, T. Bekkby, M. T. Burrows, D. F. Carlson, J.-P. Gattuso, H. Gundersen, K. Hancke, K. A. Krumhansl, T. Kuwae, J. J. Middelburg, P. J. Moore, A. M. Queiros, D. A. Smale, I. Sousa-Pinto, N. Suzuki, D. Krause-Jensen, Carbon export from seaweed forests to deep ocean sinks. *Nat. Geosci.* 17, 552–559 (2024).

- Y. Dai, S. Yang, D. Zhao, C. Hu, W. Xu, D. M. Anderson, Y. Li, X.-P. Song, D. G. Boyce, L. Gibson, C. Zheng, L. Feng, Coastal phytoplankton blooms expand and intensify in the 21st century. *Nature* 615, 280–284 (2023).
- D. Righetti, M. Vogt, N. Gruber, A. Psomas, N. E. Zimmermann, Global pattern of phytoplankton diversity driven by temperature and environmental variability. Sci. Adv. 5, eaau6253 (2019).
- D. Sun, T. Pan, S. Wang, C. Hu, Linking phytoplankton absorption to community composition in Chinese marginal seas. *Prog. Oceanogr.* 192, 102517 (2021).
- C. B. Mouw, A. Barnett, G. A. McKinley, L. Gloege, D. Pilcher, Phytoplankton size impact on export flux in the global ocean. *Global Biogeochem. Cycles* 30, 1542–1562 (2016).
- W. Y. Tang, J. Llort, J. Weis, M. M. G. Perron, S. Basart, Z. C. Li, S. Sathyendranath, T. Jackson, E. S. Rodriguez, B. C. Proemse, A. R. Bowie, C. Schallenberg, P. G. Strutton, R. Matear, N. Cassar, Widespread phytoplankton blooms triggered by 2019-2020 Australian wildfires. *Nature* 597, 370-375 (2021).
- B. B. Cael, K. Bisson, E. Boss, S. Dutkiewicz, S. Henson, Global climate-change trends detected in indicators of ocean ecology. *Nature* 619, 551–554 (2023).
- S. Dutkiewicz, A. E. Hickman, O. Jahn, S. Henson, C. Beaulieu, E. Monier, Ocean colour signature of climate change. Nat. Commun. 10, 578 (2019).
- D. G. Boyce, M. Dowd, M. R. Lewis, B. Worm, Estimating global chlorophyll changes over the past century. *Prog. Oceanogr.* 122, 163–173 (2014).
- M. L. Wells, B. Karlson, A. Wulff, R. Kudela, C. Trick, V. Asnaghi, E. Berdalet, W. Cochlan, K. Davidson, M. De Rijcke, S. Dutkiewicz, G. Hallegraeff, K. J. Flynn, C. Legrand, H. Paerl, J. Silke, S. Suikkanen, P. Thompson, V. L. Trainer, Future HAB science: Directions and challenges in a changing climate. *Harmful Algae* 91, 101632 (2020).
- C. M. Tensubam, A. V. Babanin, M. K. Dash, Fingerprints of El Niño Southern oscillation on global and regional oceanic chlorophyll-a timeseries (1997-2022). Sci. Total Environ. 955, 176893 (2024).
- E. Pauthenet, E. Martinez, T. Gorgues, J. Roussillon, L. Drumetz, R. Fablet, M. Roux, Contrasted trends in chlorophyll-a satellite products. *Geophys. Res. Lett.* 51, e2024GL 108916 (2024).
- S. Yu, Y. Bai, X. He, F. Gong, T. Li, A new merged dataset of global ocean chlorophyll-a concentration for better trend detection. Front. Mar. Sci. 10, 1051619 (2023).
- H. Zhao, M. Manizza, M. S. Lozier, N. Cassar, Greener green and bluer blue: Ocean poleward greening over the past two decades. Science 388, 1337–1340 (2025).
- Z. Li, D. Sun, S. Wang, Y. Huan, H. Zhang, Y. He, Satellites reveal hot spots of ocean changes in the early 21st century. Sci. Adv. 11, eads0307 (2025).
- N. Le Grix, J. Zscheischler, C. Laufkoetter, C. S. Rousseaux, T. L. Froelicher, Compound high-temperature and low-chlorophyll extremes in the ocean over the satellite period. *Biogeosciences* 18, 2119–2137 (2021).
- H. Hayashida, R. J. Matear, P. G. Strutton, Background nutrient concentration determines phytoplankton bloom response to marine heatwaves. Glob. Chang. Biol. 26, 4800–4811 (2020).
- K. M. Noh, H.-G. Lim, J.-S. Kug, Global chlorophyll responses to marine heatwaves in satellite ocean color. *Environ. Res. Lett.* 17, 064034 (2022).
- C. J. Gobler, Climate change and harmful algal blooms: Insights and perspective. Harmful Algae 91, 101731 (2020).
- J. Mingle, "IPCC special report on the ocean and cryosphere in a changing climate," in New York Review of Books (2020), vol. 67, pp. 49–51.
- G. M. Hallegraeff, D. M. Anderson, C. Belin, M.-Y. D. Bottein, E. Bresnan, M. Chinain, H. Enevoldsen, M. Iwataki, B. Karlson, C. H. McKenzie, I. Sunesen, G. C. Pitcher, P. Provoost, A. Richardson, L. Schweibold, P. A. Tester, V. L. Trainer, A. T. Yniguez, A. Zingone, Perceived global increase in algal blooms is attributable to intensified monitoring and emerging bloom impacts. Commun. Earth Environ. 2, 117 (2021).
- D. L. Mackas, Does blending of chlorophyll data bias temporal trend? Nature 472, E4–E5 (2011).
- M. Wang, W. Shi, L. Jiang, Atmospheric correction using near-infrared bands for satellite ocean color data processing in the turbid western Pacific region. Opt. Express 20, 741–753 (2012).
- G. Zheng, P. M. DiGiacomo, Uncertainties and applications of satellite-derived coastal water quality products. Prog. Oceanogr. 159, 45–72 (2017).
- L. Feng, C. M. Hu, Comparison of valid ocean observations between MODIS terra and aqua over the global oceans. *IEEE Trans. Geosci. Remote Sens.* 54, 1575–1585 (2016).
- X. Liu, M. Wang, Gap filling of missing data for VIIRS global ocean color products using the DINEOF method. IEEE Trans. Geosci. Remote Sens. 56, 4464

  –4476 (2018).
- K. Mikelsons, M. Wang, Optimal satellite orbit configuration for global ocean color product coverage. Opt. Express 27, A445–A457 (2019).
- A. Hilborn, M. Costa, Applications of DINEOF to satellite-derived chlorophyll-a from a productive coastal region. *Remote Sens* 10, 1449 (2018).
- L. Catipovic, F. Matic, H. Kalinic, Reconstruction methods in oceanographic satellite data observation-a survey. J. Mar. Sci. Eng. 11, 340 (2023).
- Q. Zhang, Q. Yuan, C. Zeng, X. Li, Y. Wei, Missing data reconstruction in remote sensing image with a unified spatial-temporal-spectral deep convolutional neural network. *IEEE Trans. Geosci. Remote Sens.* 56, 4274

  –4288 (2018).

# SCIENCE ADVANCES | RESEARCH ARTICLE

- D. Jin, E. Lee, K. Kwon, T. Kim, A deep learning model using satellite ocean color and hydrodynamic model to estimate chlorophyll-a concentration. *Remote Sens* 13, 2003 (2021)
- F. N. Yussof, N. Maan, M. N. M. Reba, LSTM networks to improve the prediction of harmful algal blooms in the West Coast of Sabah. Int. J. Environ. Res. Public Health 18, 7650 (2021).
- J. K. Moore, W. W. Fu, F. Primeau, G. L. Britten, K. Lindsay, M. Long, S. C. Doney,
   N. Mahowald, F. Hoffman, J. T. Randerson, Sustained climate warming drives declining marine biological productivity. Science 359, 1139–1143 (2018).
- S. X. Peng, X. L. Yu, Z. P. Lee, H. Y. Lin, X. Liu, M. H. Dai, S. L. Shang, Ocean's largest chlorophyll-rich tongue is extending westward (2002-2022). *Nat. Commun.* 16, 103 (2025)
- 40. M. Wang, C. Hu, B. B. Barnes, G. Mitchum, B. Lapointe, J. P. Montoya, The great Atlantic Sargassum belt. *Science* **365**, 83–87 (2019).
- R. G. Pearson, N. M. Connolly, A. M. Davis, J. E. Brodie, Fresh waters and estuaries of the Great Barrier Reef catchment: Effects and management of anthropogenic disturbance on biodiversity, ecology and connectivity. *Mar. Pollut. Bull.* 166, 112194 (2021).
- C. Karnan, S. Gautham, Seasonal enhancement of phytoplankton biomass in the southern tropical Indian Ocean: Significance of meteorological and oceanography parameters. *Oceanologia* 66, 196–219 (2024).
- M. J. Behrenfeld, R. T. O'Malley, E. S. Boss, T. K. Westberry, J. R. Graff, K. H. Halsey, A. J. Milligan, D. A. Siegel, M. B. Brown, Revaluating ocean warming impacts on global phytoplankton. *Nat. Clim. Chang.* 6, 323–330 (2016).
- S. Sun, A. F. Thompson, J. Yu, L. Wu, Transient overturning changes cause an upper-ocean nutrient decline in a warming climate. *Nat. Commun.* 15, 7727–7727 (2024).
- 45. G. C. Li, L. J. Cheng, J. Zhu, K. E. Trenberth, M. E. Mann, J. P. Abraham, Increasing ocean stratification over the past half-century. *Nat. Clim. Chang.* **10**, 1116–1123 (2020).
- J.-B. Sallee, V. Pellichero, C. Akhoudas, E. Pauthenet, L. Vignes, S. Schmidtko, A. N. Garabato, P. Sutherland, M. Kuusela, Summertime increases in upper-ocean stratification and mixed-layer depth. *Nature* 596, E7–E7 (2021).
- G. Mataveli, G. de Oliveira, C. H. L. Silva-Junior, S. C. Stark, N. Carvalho, L. O. Anderson, L. V. Gatti, L. E. O. C. Aragao, Record-breaking fires in the Brazilian Amazon associated with uncontrolled deforestation. *Nat. Ecol. Evol.* 6, 1792–1793 (2022).
- M. J. Behrenfeld, P. G. Falkowski, Photosynthetic rates derived from satellite-based chlorophyll concentration. *Limnol. Oceanogr.* 42, 1–20 (1997).
- A. Capotondi, R. R. Rodrigues, A. Sen Gupta, J. A. Benthuysen, C. Deser, T. L. Froelicher, N. S. Lovenduski, D. J. Amaya, N. Le Grix, T. Xu, J. Hermes, N. J. Holbrook, C. Martinez-Villalobos, S. Masina, M. K. Roxy, A. Schaeffer, R. W. Schlegel, K. E. Smith, C. Wang, A global overview of marine heatwaves in a changing climate. *Commun. Earth Environ.* 5, 701 (2024).
- E. C. J. Oliver, M. T. Burrows, M. G. Donat, A. Sen Gupta, L. V. Alexander,
   E. Perkins-Kirkpatrick, J. A. Benthuysen, A. J. Hobday, N. J. Holbrook, P. J. Moore,
   M. S. Thomsen, T. Wernberg, D. A. Smale, Projected marine heatwaves in the 21st century and the potential for ecological impact. Front. Mar. Sci. 6, 734 (2019).
- E. N. Dethier, C. E. Renshaw, F. J. Magilligan, Rapid changes to global river suspended sediment flux by humans. Science 376, 1447–1452 (2022).
- D. Feng, C. J. Gleason, More flow upstream and less flow downstream: The changing form and function of global rivers. Science 386, 1305–1311 (2024).
- C. Hu, L. Feng, Modified MODIS fluorescence line height data product to improve image interpretation for red tide monitoring in the eastern Gulf of Mexico. J. Appl. Remote Sens. 11, 012003 (2016)
- F. Shen, R. Tang, X. Sun, D. Liu, Simple methods for satellite identification of algal blooms and species using 10-year time series data from the East China Sea. *Remote Sens. Environ.* 235, 111484 (2019).
- D. B. van de Waal, A. M. Verschoor, J. M. H. Verspagen, E. van Donk, J. Huisman, Climate-driven changes in the ecological stoichiometry of aquatic ecosystems. Front. Ecol. Environ. 8, 145–152 (2010).
- D. Zhai, C. Beaulieu, R. M. Kudela, Long-term trends in the distribution of ocean chlorophyll. *Geophys. Res. Lett.* 51, e2023GL106577 (2024).
- Y. Wu, L. Feng, X. Liu, Y. Wang, C. Zheng, Declining phytoplankton biomass in Chinese Coastal oceans linked to climate warming. *Environ. Sci. Technol.* 59, 11607–11615 (2025).
- T. K. Westberry, M. J. Behrenfeld, Y. R. Shi, H. Yu, L. A. Remer, H. Bian, Atmospheric nourishment of global ocean ecosystems. Science 380, 515–519 (2023).
- X. Liu, M. Wang, Global daily gap-free ocean color products from multi-satellite measurements. Int. J. Appl. Earth Obs. Geoinf. 108, 102714 (2022).
- H. Lavigne, D. Van der Zande, K. Ruddick, J. F. C. Dos Santos, F. Gohin, V. Brotas, S. Kratzer, Quality-control tests for OC4, OC5 and NIR-red satellite chlorophyll-a algorithms applied to coastal waters. *Remote Sens. Environ.* 255, 112237 (2021).
- Z. K. Hong, D. Long, X. D. Li, Y. M. Wang, J. M. Zhang, M. A. Hamouda, M. M. Mohamed, A global daily gap-filled chlorophyll-a dataset in open oceans during 2001-2021 from multisource information using convolutional neural networks. *Earth Syst. Sci. Data* 15, 5281–5300 (2023).

- M. Karydis, F. Chatzichristofas, "Coastal eutrophication in the Mediterranean marine environment: A short review," in 8th International Conference on Environmental Science and Technology (Lemnos Isl, 2003), pp. 426–430.
- R. L. Miller, B. A. McKee, Using MODIS Terra 250 m imagery to map concentrations of total suspended matter in coastal waters. *Remote Sens. Environ.* 93, 259–266 (2004).
- 64. S. Sathyendranath, R. Brewin, C. Brockmann, V. Brotas, B. Calton, A. Chuprin, P. Cipollini, A. Couto, J. Dingle, R. Doerffer, C. Donlon, M. Dowell, A. Farman, M. Grant, S. Groom, A. Horseman, T. Jackson, H. Krasemann, S. Lavender, V. Martinez-Vicente, C. Mazeran, F. Mélin, T. Moore, D. Müller, P. Regner, S. Roy, C. Steele, F. Steinmetz, J. Swinton, M. Taberner, A. Thompson, A. Valente, M. Zühlke, V. Brando, H. Feng, G. Feldman, B. Franz, R. Frouin, R. Gould, S. Hooker, M. Kahru, S. Kratzer, B. Mitchell, F. Muller-Karger, H. Sosik, K. Voss, J. Werdell, T. Platt, An ocean-colour time series for use in climate studies: The experience of the Ocean-Colour Climate Change Initiative (OC-CCI). Sensors 19, 4285 (2019).
- Y. Han, Y.T. Zhou, Investigating biophysical control of marine phytoplankton dynamics via Bayesian mechanistic modeling. *Ecol. Model.* 474, 110168 (2022).
- N. G. Nelson, R. Munoz-Carpena, E. Phlips, Parameter uncertainty drives important incongruities between simulated chlorophyll-a and phytoplankton functional group dynamics in a mechanistic management model. *Environ. Model. Software* 129, 104708 (2020).
- 67. H. Hersbach, B. Bell, P. Berrisford, S. Hirahara, A. Horanyi, J. Munoz-Sabater, J. Nicolas, C. Peubey, R. Radu, D. Schepers, A. Simmons, C. Soci, S. Abdalla, X. Abellan, G. Balsamo, P. Bechtold, G. Biavati, J. Bidlot, M. Bonavita, G. De Chiara, P. Dahlgren, D. Dee, M. Diamantakis, R. Dragani, J. Flemming, R. Forbes, M. Fenetes, A. Geer, L. Haimberger, S. Healy, R. J. Hogan, E. Holm, M. Janiskova, S. Keeley, P. Laloyaux, P. Lopez, C. Lupu, G. Radnoti, P. de Rosnay, I. Rozum, F. Vamborg, S. Villaume, J. N. Thepaut, The ERA5 global reanalysis. Q. J. Roy. Meteorol. Soc. 146, 1999–2049 (2020).
- H. Zuo, M. A. Balmaseda, S. Tietsche, K. Mogensen, M. Mayer, The ECMWF operational ensemble reanalysis-analysis system for ocean and sea ice: A description of the system and assessment. *Ocean Sci.* 15, 779–808 (2019).
- X. Xing, E. Boss, Chlorophyll-based model to estimate underwater photosynthetically available radiation for modeling, in-situ, and remote-sensing applications. *Geophys. Res.* Lett. 48, e2020GL092189 (2021).
- V. Di Biagio, G. Cossarini, S. Salon, C. Solidoro, Extreme event waves in marine ecosystems: An application to Mediterranean Sea surface chlorophyll. *Biogeosciences* 17, 5967–5988 (2020)
- A. J. Hobday, L. V. Alexander, S. E. Perkins, D. A. Smale, S. C. Straub, E. C. J. Oliver, J. A. Benthuysen, M. T. Burrows, M. G. Donat, M. Peng, N. J. Holbrook, P. J. Moore, H. A. Scannell, A. Sen Gupta, T. Wernberg, A hierarchical approach to defining marine heatwaves. *Prog. Oceanogr.* 141, 227–238 (2016).
- L. Catipovic, S. Sathyendranath, F. Matic, Z. Kovac, L. Kovacic, Z. N. Gladan, S. Skejic, H. Kalinic, Sources of uncertainty in satellite-derived chlorophyll-a concentration—An Adriatic Sea case study. *Int. J. Appl. Earth Obs. Geoinf.* 128, 103727 (2024).
- J. Park, S. Khanal, K. G. Zhao, K. Byun, Remote sensing of chlorophyll-a and water quality over inland lakes: How to alleviate geo-location error and temporal discrepancy in model training. *Remote Sens* 16, 2761 (2024).
- W. C. Xie, T. Wang, W. S. Jiang, Spatio-temporal variability of surface chlorophyll a in the Yellow Sea and the East China Sea based on reconstructions of satellite data of 2001-2020. J. Oceanol. Limnol. 42, 390–407 (2024).
- V. Agarwal, J. Chávez-Casillas, K. Inomura, C. B. Mouw, Patterns in the temporal complexity of global chlorophyll concentration. Nat. Commun. 15, 1522 (2024).
- Y. H. Ahn, P. Shanmugam, J. H. Ryu, J. C. Jeong, Satellite detection of harmful algal bloom occurrences in Korean waters. Harmful Algae 5, 213–231 (2006).
- K. Sherman, Adaptive management institutions at the regional level: The case of large marine ecosystems. Ocean Coast. Manag. 90, 38–49 (2014).
- Y. Liu, R. H. Weisberg, J. M. Lenes, L. Zheng, K. Hubbard, J. J. Walsh, Offshore forcing on the "pressure point" of the West Florida Shelf: Anomalous upwelling and its influence on harmful algal blooms. J. Geophys. Res. Oceans 121, 5501–5515 (2016).
- Y. Xu, Y. Sun, H. Xiao, B. Ai, D. Liu, Remote sensing identification of red tide in Pearl River Estuary based on hue angle algorithm. *Acta Sci. Nat. Univ. Sunyatseni* 63, 96–104 (2024).

Acknowledgments: We thank the researchers and the teams for providing all the datasets used in this study. We also thank the reviewers and editors for suggestions, which significantly improved the quality of this study and manuscript. Funding: This work was supported by the National Natural Science Foundation of China grant 52325901 (D.L.) and the UKRI Natural Environment Research Council (NERC) Independent Research Fellowship grant NE/T011246/1 (R.I.W.). Author contributions: Conceptualization: D.L., K.S., J.-M.Z., and H.F. Methodology: Z.H., D.L., and K.S. Software: Z.H. and D.L. Validation: Z.H., D.L., K.S., J.-M.Z., R.I.W., M.L., M.E.M., and H.F. Investigation: Z.H., D.L., K.S., J.-M.Z., R.I.W., M.L., M.E.M., and H.F. Data curation: D.L., J.-M.Z., and H.F. Writing—original draft: Z.H., D.L., K.S., J.-M.Z., R.I.W., M.L., M.E.M., and H.F.

# SCIENCE ADVANCES | RESEARCH ARTICLE

Writing—review and editing: Z.H., D.L., K.S., J.-M.Z., R.I.W., M.L., M.E.M., and H.F. Visualization: Z.H., D.L., and K.S. Supervision: D.L. J.-M.Z., and H.F. Project administration: D.L. and R.I.W. Funding acquisition: D.L. and R.I.W. **Competing interests:** The authors declare that they have no competing interests. **Data and materials availability:** All data needed to evaluate the conclusions in the paper are present in the paper and/or the Supplementary Materials. The global daily Chl-a concentration dataset with a 0.25° by 0.25° resolution, generated using the OCNET model, along with the corresponding associated code and the dataset of MHC events,

is available at https://doi.org/10.5281/zenodo.14691522. All relevant source data are provided with this paper.

Submitted 16 March 2025 Accepted 15 September 2025 Published 17 October 2025 10.1126/sciadv.adx4857